Faraday Discussions

Accepted Manuscript

This manuscript will be presented and discussed at a forthcoming Faraday Discussion meeting. All delegates can contribute to the discussion which will be included in the final volume.

Register now to attend! Full details of all upcoming meetings: http://rsc.li/fd-upcoming-meetings

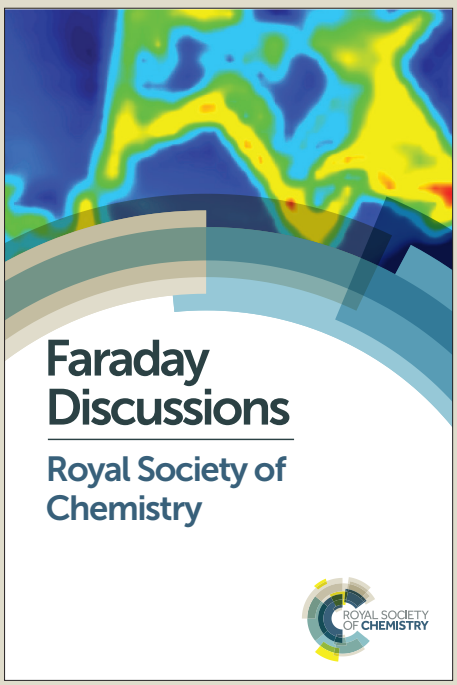

This is an *Accepted Manuscript*, which has been through the Royal Society of Chemistry peer review process and has been accepted for publication.

Accepted Manuscripts are published online shortly after acceptance, before technical editing, formatting and proof reading. Using this free service, authors can make their results available to the community, in citable form, before we publish the edited article. We will replace this *Accepted Manuscript* with the edited and formatted *Advance Article* as soon as it is available.

You can find more information about *Accepted Manuscripts* in the Information for Authors.

Please note that technical editing may introduce minor changes to the text and/or graphics, which may alter content. The journal's standard Terms & Conditions and the Ethical guidelines still apply. In no event shall the Royal Society of Chemistry be held responsible for any errors or omissions in this *Accepted Manuscript* or any consequences arising from the use of any information it contains.

ROYAL SOCIETY OF CHEMISTRY

www.rsc.org/faraday_d

A comparative study of CO adsorption on tetrahexahedral Pt nanocrystals and interrelated Pt single crystal electrodes by using cyclic voltammetry and in-situ FTIR spectroscopy

Hai-Xia Liu, Na Tian*, Jin-Yu Ye, Bang-An Lu, Jie Ren, Zhi-Chao Huangfu, Zhi-You Zhou, Shi-Gang Sun*

State Key Lab of Physical Chemistry of Solid Surfaces, Department of Chemistry, College of Chemistry and Chemical Engineering, XiamenUniversity, Xiamen, 361005, China,

E-mail: tnsd@xmu.edu.cn, sgsun@xmu.edu.cn

Abstract:

This study focuses on CO adsorption at tetrahexahedral Pt nanocrystals (THH Pt NCs) by using cyclic voltammetry and in-situ FTIR spectroscopy. Since the electrochemically prepared THH Pt NCs in this study are enclosed by {730} facets which could be considered by a subfacet configuration of 2{210}+{310}, we have studied also CO adsorption on the interrelated Pt(310) and Pt(210) single crystal electrodes as comparison. Cyclic voltammetry results demonstrated that CO adsorbs dominantly on (100) sites of THH Pt NCs at low CO coverage ($\theta_{CO} \leq 0.135$), while on both (100) and (110) sites at higher CO coverage. On ordered Pt(310) and Pt(210), i.e. they were flame annealed and then cooled in H_2 + Ar, CO adsorption also illustrates relative priority on (100) sites at low CO coverage; while at high CO coverage or on oxygen-disordered Pt(310) and Pt(210) when they were cooled in air after flame annealing, the adsorption of CO presents a weak preference on (100) sites of Pt(310) and even no preference at all on (100) sites of Pt(210). In-situ FTIR spectroscopic studies illustrated that CO adsorption on THH Pt NCs yields anomalous infrared effects (AIREs), which depicted by the Fano-like IR feature on a dense distribution (60 μm^{-2}) and the enhancement of abnormal IR absorption on a sparse distribution (22 μm^{-2}) of THH Pt NCs on glassy carbon substrate. Systematic investigation of CO overage dependence of IR features revealed that, on THH Pt NCs, the IR band center (ν_{COL}) of linearly bonded CO (CO_L) is

rapidly shifted to higher wavenumbers along with the increase of CO coverage till 0.184, yielding a fast linear increase rate of a big slop ($d\nu_{COL} / d\theta_{CO}^{IR}$ = 219 cm^{-1}); when θ_{CO}^{IR} > 0.184, the increase of ν_{COL} with θ_{CO} is slowing down and deviated drastically from the linearity. On the contrast, the ν_{COL} on the ordered Pt(310) electrode keeps a linear increase with θ_{CO}^{IR} for the whole range of θ_{CO}^{IR} variation, and gives a much smaller increase rate of slop 74.3 cm^{-1}. The significant differences in CO adsorption behaviors on THH Pt NCs and on interrelated Pt single crystal planes demonstrated clearly the unique properties of nanoparticles enclosed by high-index facets.

Keywords: THH Pt NCs, Pt(310), Pt(210), CO adsorption, Cyclic voltammetry, in-situ FTIR spectroscopy

1. Introduction

High-index faceted metal nanocrystals have received great attention due to their high catalytic activity originated from high density of low-coordinated step atoms on their surface.[1, 2] In last years, we have devoted to synthesize high-index faceted metal nanocrystals through developing electrochemical methods, in which the square-wave potential (SWP) method owns a unique advantage of synthesizing metal nanocrystals of high surface energy.[3] Our systematic studies led to the success of preparation of a series of Pt-group metal catalysts enclosed with high-index facets, including (1) the tetrahexahedral metal nanocrystals (THH metal NCs) with {hk0} high-index facets, such as THH Pt NCs,[3] THH Pd NCs[4] and THH Rh NCs;[5] (2) the trapezohedral metal nanocrystals (TPH metal NCs) with {hkk} high-index facets, such as TPH Pt NCs[6] and TPH Pd NCs;[7] (3) the hexoctahedral Pt nanocrystals (HOH Pt NCs) with{hkl} high-index facets;[8] (4) the Pd- and Pt-based alloy metal nanocrystals with high index facets, such as THH PdPt NCs,[9] THH PtRh NCs and TPH PtRh NCs.[10] In the SWP method, the parameters that govern the composition, the type of high-index facets and the size of high-index faceted metal nanocrystals consist mainly the metal precursors and their concentration in solution, the SWP (the frequency, the upper and lower limit potentials), and the growth time. Generally, the high-index facets are

mainly created by the repetitive adsorption/desorption of oxygen species mediated by the SWP[3].The growth rate of nanocrystals is controlled mainly by the lower limit potential. As for different metals, the upper and lower limit potentials of the SWP should be adjusted and optimized on basis of the adsorption/desorption behavior of oxygen species on them. Usually, the upper limit potential for Pt (1.0~1.20 V vs SCE) is significantly higher than that for Pd and Rh (about 0.70 V), because the latter two elements can be oxidized at lower potentials and the formed oxygen species on them are more difficult to be reduced electrochemically than that on Pt.

Although the Miller index that represents the atomic arrangement of the facets of high-index faceted metal nanocrystals can be determined by transmission electron microscopy (TEM), the real surface structure and its evolution under chemical conditions is less studied though it is most important for understanding the origin of the excellent catalytic properties of high-index faceted metal nanocrystals. The most frequently prepared THH Pt NCs by electrochemically shape-controlled synthesis are bounded with {730} facets.[3, 8] It is known that a single crystal plane with (730) index could be considered as a subfacet configuration of 2(210) + (310), i.e. it contains periodically two (210) subfacets and one (310) subfacet. Although the surface structure-catalytic functionality of metal single crystal planes used as model electrocatalyst has been extensively investigated, especially in case of platinum group metals,[11-13] the surface structure-catalytic functionality of metal nanoparticles employed as real catalysts in industrial applications is far from understand. The shape-control synthesized metal nanoparticles, such as the THH Pt NCs, expose smooth facets with well-defined surface atomic structure as single crystal planes, while hold the nanometer particle size, and the particular corner and edge sites. So, the surface structure of nanoparticle is more complex, which could consequently lead to very different properties of the nanoparticles from the interrelated single crystal planes with the same atomic structure of facets that enclose the nanoparticles.

CO is one of most attractive molecule in electrocatalysis due to the following reasons: i) CO is the poisonous intermediate involved in oxidation or dissociation of most organic molecule fuels;[14, 15] ii) The blank $2\pi^*$ orbital of CO can accept *d*-electrons from transition metals to form *d*-π^* back-donation bond, enhancing consequently the interaction between CO and Pt sites;[16, 17] iii) CO electrooxidation is surface structure sensitive reaction.[18, 19] Due to the strong interaction between CO and Pt, CO usually serves as a probe molecule to detect the surface active sites of Pt

catalysts.

It has reported that, for CO absorption on basal planes of Pt single crystal, the bridge-bonded CO (CO_B) is favorable on Pt(111) and Pt(100) in both electrochemical and UHV conditions at low coverage,[20] while the linearly-bonded CO (CO_L) is dominant on the Pt(110) single crystal electrode.[20, 21] Most of studies concerning CO absorbed on Pt high-index planes indicate that CO prefers to adsorb on steps, but CO randomly adsorbs on steps and terraces in the surface of Pt (S) [n(111) × (110)] single crystal planes.[22]

In the current study, we employ CO as probe molecule to investigate the surface sites on THH Pt NCs by cyclic voltammetry (CV) and in-situ FTIR spectroscopy. The results are compared with interrelated Pt(210) and Pt(310) single crystal planes, in order to understand the unique properties of the THH Pt NCs.

2. Experimental

2.1 Materials and apparatus

H_2PtCl_6 (99.99%, Sigma Aldrich), sulfuric acid (96%, Merck), perchloric acid (super pure) were used as received. All solutions were prepared using super pure water (18 MΩ·cm) generated from a Milli-Q system (Nihon Millipore Ltd.). Carbon monoxide gas (99.99%) was purchased from Xiamen Xinhang Co.

THH Pt NCs was electrochemically prepared on glassy carbon (GC) electrode (Φ = 6 mm) by using the same procedure described in our previous work.[3] Prior to deposit THH Pt NCs, the GC was polished mechanically by using successively alumina powder of sizes 5, 1, 0.3 μm, and finally cleaned in an ultrasonic bath. The counter electrode and reference electrode are platinum foil and a saturated calomel electrode (SCE), respectively. The electrochemical experiments were carried out in a standard three electrode cell at room temperature (~25°C). Potential control was achieved with a PAR 263A potentiostat/galvanostat operated through home-developed software.

All solutions were purged with bubbling pure N_2 gas (99.99%) for 15 min before experiments. A nitrogen gas flow was maintained above the solution during measurement to prevent interference of atmospheric oxygen and impurities.

2.2 Preparation of THH Pt nanocrystals

THH Pt NCs was prepared by using a square-wave potential method.[10] Briefly, THH Pt NCs were deposited on GC electrode by applying a potential step from 1.20 V to a reduction potential of −0.30 V, holding for 0.14 s in 1.93 mM H_2PtCl_6 + 0.1 M H_2SO_4 solution. A square wave potential of frequency 100 Hz with lower potential 0.03 V and upper potential 1.06 V was applied for 20 min to grow up the THH Pt NCs. The deposited THH Pt NCs was characterized by cyclic voltammetry in 0.1 M H_2SO_4 solution and then imaged by scanning electron microscopy (SEM, Hitachi S-4800).

2.3 Preparation of Pt single crystal electrodes

Platinum single crystal beads were oriented, cut and polished according to Clavilier's method.[23] The electrode was annealed in a H_2-O_2 flame at about 1200°C making it clean and ordered, and then cooled down to the room temperature in H_2 + Ar flow or air (atmosphere). The flame treated electrode was immediately transferred into electrochemical cell or in-situ FTIR spectroelectrochemical cell with its surface protected by super pure water for further investigation.

2.4 CO adsorption experiments

The THH Pt NCs electrode was placed in a 0.1 M H_2SO_4 solution. In order to obtain a low CO coverage, with the electrode potential held at –0.10 V CO gas was bubbled through the solution. The CO coverage was controlled by adjusting the time of CO bubbling. The CO supply was then turned off and N_2 gas was introduced to purge the solution for 10 min in order to remove completely dissolved CO in solution. Finally, oxidation of the adsorbed CO (CO_{ad}) was investigated by cyclic voltammetry. The electrode potential was scanned starting from the initial potential of –0.10 V down to –0.25 V, and then a complete cyclic voltammogram with an upper limit of 0.75 V was recorded. The scan rate was 50 $mV.s^{-1}$.

The coverage of CO (θ_{CO}) was calculated by the charge of CO_{ad} oxidation to that of one monolayer CO_{ad} oxidation, and was defined as:

$$\theta_{CO} = \frac{Q^{CO}}{Q^{CO}_{1ML-CO}} \quad (1)$$

Where Q^{CO} and Q^{CO}_{1ML-CO} are the charges of CO_{ad} oxidation of the sub monolayer CO_{ad} and one monolayer CO_{ad}, respectively. It is worthwhile noting that this definition stands for the ratio of adsorbed CO versus the saturation adsorption of a CO_{ad} monolayer.

The procedure of yielding different coverage of CO absorbed on Pt single crystal electrodes was similar with that of CO absorption on the THH Pt NCs. In order to prevent the perturbation of surface atomic structure at high electrode potentials, the cyclic potential range was limited between –0.25 and 0.60 V in cyclic voltammetry studies of Pt single crystal electrodes.

The electrochemical active surface area (ECSA) of the THH Pt NCs electrode was measured according the method reported in the literature[24] through ECSA = Q_H / (210μC·cm^{-2}), where Q_H is the charge of hydrogen desorption by integration of the CV curve recorded in 0.1 H_2SO_4 solution between –0.25 to 0.15 V.

2.5 Electrochemical in-situ FTIR reflection spectroscopy

In-situ FTIR spectroscopy experiments were carried out on a Nexus 870 FTIR spectrometer (Nicolet) equipped with a liquid-nitrogen-cooled MCT−A detector. A thin layer in-situ FTIIR cell with CaF_2 window was utilized [25]. A total 400 single-beams at resolution of 2 cm^{-1} were co-added to increase the signal-to-noise ratio. The in-situ FTIR spectra of various coverage of CO_{ad} was measured using the following procedure: i) holding the potential at −0.10 V, bubbling a few bubbles of CO; ii) after removing completely dissolved CO in solution by bubbling N_2, the electrode was pushed to the window and the sample spectra were collected at a series sample potentials E_S; iii) The reference spectrum was acquired finally at E_R (0.75 V for THH Pt NCs, and 0.60 V for Pt single crystal electrodes), at which potential the adsorbed CO is oxidized completely. The resulting spectra were reported as relative change in reflectivity, that is,

$$\frac{\Delta R}{R}(E_S) = \frac{R(E_S) - R(E_R)}{R(E_R)} \quad (2)$$

where $R(E_S)$ and $R(E_R)$ are single-beam spectra collected at the sample potential E_S and

reference potential E_R, respectively.

3 Results and discussions

3.1 Cyclic voltammetry studies

Fig. 1A shows the SEM image of THH Pt NCs with a distribution density of about 60 μm^{-2}. The high magnification SEM image is shown in the inset (a). The surface facets of the THH Pt NCs prepared under present conditions are mainly {730} facets,[8] which can be denoted as 2(210) + (310) or 3(100) × (110) + 2(100) × (110). The inset (b) is an atomic model of a THH Pt NC enclosed with {730} facets. The size distribution histogram of THH Pt NCs in Fig. 1B indicates that the mean size is about 54 nm.

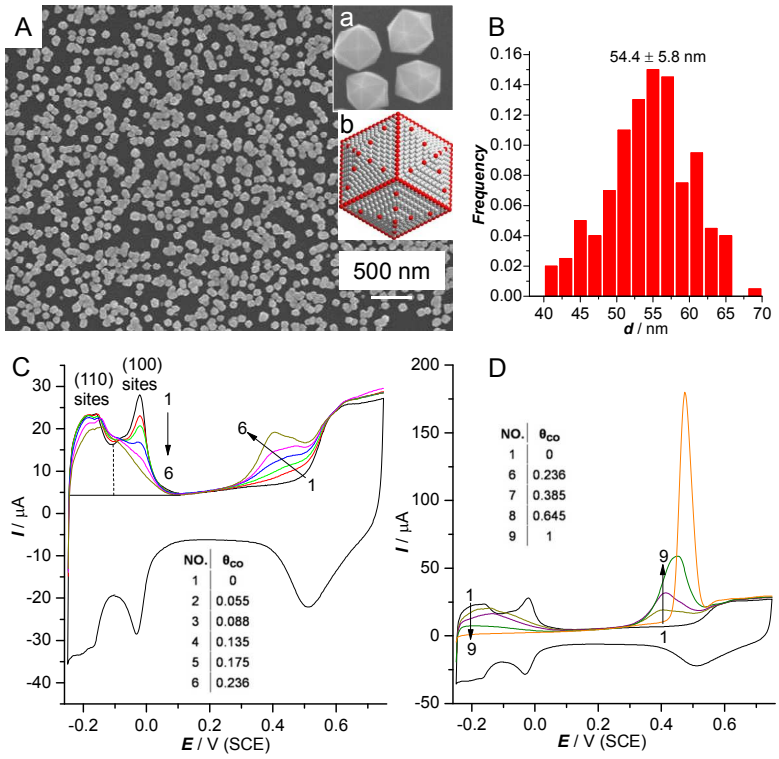

Fig. 1 (A) SEM image of THH Pt NCs. The inset (a) is a high magnification image of the sample, which illustrates clearly the THH shape, and the inset (b) depicts the atomic model of a THH Pt NC with {730} facets. (B) Size distribution histogram for the THH Pt NCs by counting 200 nanoparticles. (C and D) CV curves of CO stripping on THH Pt NCs electrodes with different CO coverage, in 0.1 M H_2SO_4 solution, scan rate 50 $mV.s^{-1}$.

Fig. 1C and D illustrate the CV curves of CO_{ad} stripping on THH Pt NCs at various CO_{ad} coverages. From the features of hydrogen adsorption-desorption on a clean THH Pt NCs ($\theta_{CO} = 0$), two potential regions may be discerned. One is the potential region between −0.25 V and −0.106 V for hydrogen desorption on (110) sites, another potential region is from −0.106 V to 0.15V for hydrogen desorption on (100) sites. We can observe from Fig. 1C that the hydrogen desorption peak at around −0.02 V (corresponding to Pt(100) sites) is blocked faster than that at −0.16 V (corresponding to Pt(110) sites). At low CO coverage ($\theta_{CO} \leq 0.135$), the peak at −0.02 V was blocked obviously, while the peak at −0.16 V almost keeps unblocked. This implies that CO adsorbs dominantly on Pt(100) sites at such a low CO_{ad} coverage. When $\theta_{CO} \geq 0.175$, CO adsorbs on both Pt(100) sites and (110) sites as illustrated by the simultaneous blocking of both hydrogen adsorption peaks.

Voltammogram of the THH Pt NCs ($\theta_{CO} = 0$) presented in Fig. 1C exhibits a strong peak for oxygen adsorption around 0.6 V with its onset potential at 0.46 V. However, for the stripping of CO_{ad} with low coverage, the onset potential of CO_{ad} oxidation is measured at about 0.27 V, which is negatively shifted by about 0.19 V than the onset potential of Pt−OH formation on the surface of THH Pt NCs. This may attribute to the adsorption of H_2O on Pt(110) step sites that promoted the oxidation CO adsorbed on Pt(100) sites. Lebedeva et al. have studied in detail CO stripping on a series of Pt(S) [n(111) × (110)] single crystal electrodes in acidic media,[26, 27] and demonstrated that the rate constant for CO_{ad} oxidation is a linear function of the step density, suggesting that indeed OH_{ad} formation occurs preferentially on the (110) steps. A previous study[28] of CO_{ad} monolayer oxidation on stepped Pt(s) [(n-1)(100) × (110)] surfaces indicated that for the short terraces (n < 7) the CO_{ad} oxidation peak shifts toward lower potential as the step density increase, and for the long terraces (n > 7) the result is reverse. On the THH Pt NCs enclosed by {730} facets, the value of n is small than 7, so the results of the high activity for CO_{ad} oxidation is consistent with the literature results. As illustrated in Fig. 1D, the onset potential and the peak potential are both shifted toward higher potential along with increasing the CO coverage. It can observe that the oxidation of a monolayer CO_{ad} gives a small per-oxidation current between 0.32~0.41V, and a large and sharp current peak at about 0.475 V.

To understand the surface structure effect of the THH Pt NCs, we investigated the behavior of

CO adsorption on interrelated Pt single crystal electrodes. Fig. 2 shows the cyclic voltammograms of hydrogen desorption potential region (−0.25 ~ 0.15V) recorded on ordered (cooled in H_2 + Ar) and oxygen-disordered (cooled in air) Pt(210) and Pt (310) single crystal electrodes at different CO_{ad} coverage, respectively. It is known that the surface cooled in air is usually less ordered than that cooled in H_2 + Ar, since the oxygen adsorption can induce surface defects[29]. We observe from Fig. 2 that CO adsorption can suppress the hydrogen desorption current on both (100) and (110) sites for the whole CO_{ad} coverage. This is different from that on THH Pt NCs, which show a dominant preferential adsorption on (100) sites at low CO coverage of $\theta_{CO} \leq 0.135$.

We can use the ratio of hydrogen desorption charge between −0.25 and −0.106V over the total hydrogen desorption charge to estimate approximately the proportion of (110) sites, and that between −0.106 and 0.15 V for the proportion of (100) sites on the clean surface of the THH Pt NCs, i.e. $\theta_{CO} = 0$. The experimental result indicates a proportion of (110) sites at 51%, which is slightly larger than that from theoretical calculation of a Pt(730) single crystal plane (43%). This may be caused by corner and edge atoms on the THH Pt NCs. For the Pt(210) and Pt(310) cooled in air, the proportions of CO_{ad} blocked (110) sites and (100) sites were measured from the hydrogen adsorption charges in the region between −0.25 and −0.106V and that between −0.106 and 0.15V (the separation potential −0.106 corresponding to the lowest current between the two regions) over the total hydrogen adsorption charge; and for Pt(310) and Pt(210) cooled in H_2 + Ar, the proportions of CO_{ad} blocked (110) sites and (100) sites were measured from the hydrogen desorption charges in the region between −0.25 and −0.114V and that between −0.114 and 0.15V over the total hydrogen adsorption charge. The results were nearly 1:1 ((110):(100)) for Pt(210) and 1:2 for Pt(310), respectively, which are the same as those from theoretical calculation of these two single crystal planes.

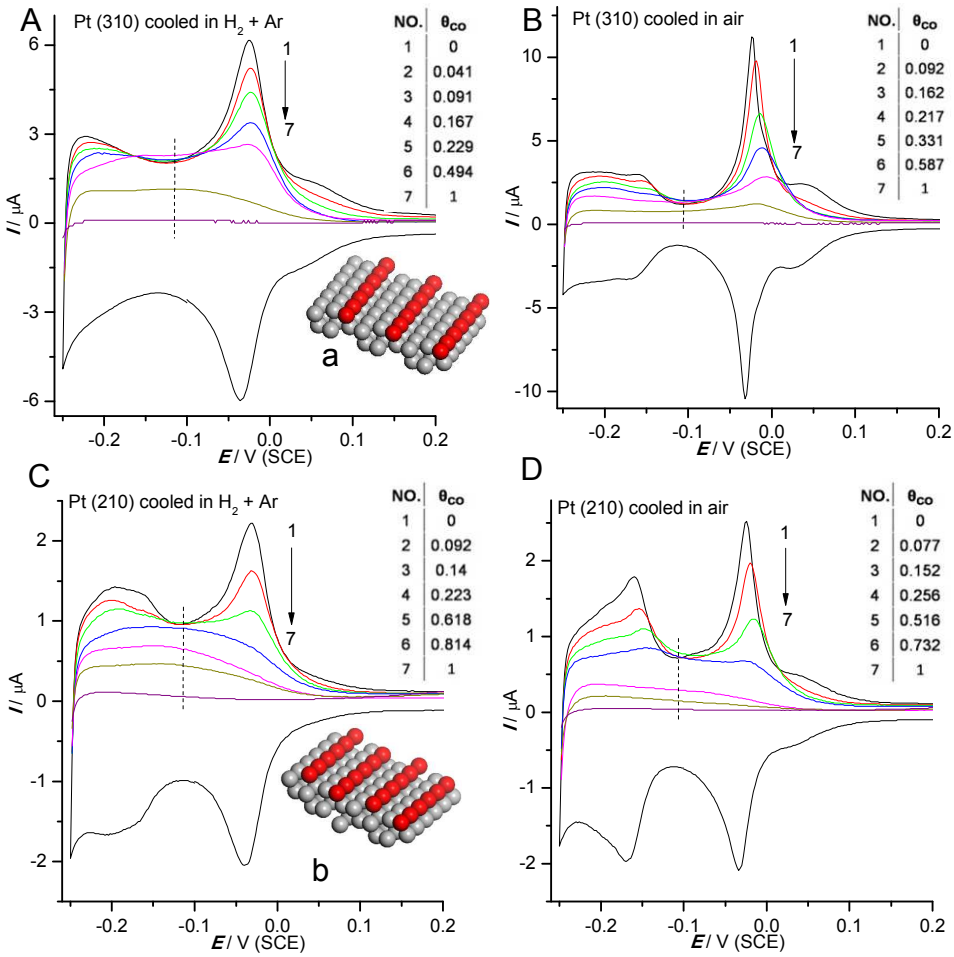

Fig. 2 Cyclic voltammograms of hydrogen adsorption region for Pt(210) and Pt(310) single crystal electrodes at different CO coverage. (A) Pt(310) cooled in H_2 + Ar; (B) Pt(310) cooled in air; (C) Pt(210) cooled in H_2 + Ar; (D) Pt(210) cooled in air. 0.1 M H_2SO_4 solution, scan rate 50 $mV.s^{-1}$. The insets represent the atomic models of Pt(310) (a) and Pt(210) (b), in which the red atoms are the (110) steps and the gray ones are (100) terraces.

In order to analyze the preferential adsorption of CO on the (100) sites clearly, we define the proportion of (100) sites ($\eta_{(100)\ sites}$) and (110) sites ($\eta_{(110)\ sites}$) that are blocked by adsorbed CO at various CO coverage on THH Pt NCs and Pt(210), Pt(310) single crystal electrodes. The blocked (110) sites and (100) sites by CO adsorption was obtained by subtracting the hydrogen desorption charge integrated from the CV curves of corresponding potentials regions mentioned above before CO stripping from that after CO stripping. The proportion ($\eta_{(hk0)\ sites}$) of CO-blocked (100) or (110) sites was calculated by CO blocked (100) sites (or (110) sites) over the total (100) sites (or (110)

sites) as:

$$\eta_{(hk0)-sites} = \frac{Q^{H}_{(1k0)\ sites} - Q^{H}_{(1k0)\ sites-CO}}{Q^{H}_{(1k0)\ sites}} = 1 - \frac{Q^{H}_{(1k0)\ sites-CO}}{Q^{H}_{(1k0)\ sites}} \quad (k=1 \text{ or } 0) \qquad (3)$$

Where $Q^{H}_{(1k0)\ sites-CO}$ is the charge of hydrogen desorption on (1k0) sites with adsorbed CO, $Q^{H}_{(1k0)\ sites}$ is the charge of hydrogen desorption on (1k0) sites after CO_{ad} stripping without any CO adsorption.

The results in Fig. 3 A indicate that, on THH Pt NCs, the $\eta_{(100)\ sites}$ is about 0.084, 0.117 and 0.192 corresponding respectively to θ_{co} at 0.055, 0.088 and 0.135, and $\eta_{(110)\ sites}$ is always near zero at these low CO coverage, indicating that CO adsorbed predominantly on (100) sites at such a low CO coverage ($\theta_{co} \leq 0.135$); Following the increase of θ_{co} to 0.175, the $\eta_{(110)\ sites}$ begins increasing; Further increasing CO coverage, both $\eta_{(100)\ sites}$ and $\eta_{(110)\ sites}$ increase rapidly, but $\eta_{(100)\ sites}$ is always slightly bigger than $\eta_{(110)\ sites}$ for all θ_{co} except $\theta_{co} = 1$, at which $\eta_{(100)\ sites}$ equals to $\eta_{(110)\ sites}$. These results suggest that CO adsorption has always the preference on (100) sites of THH Pt NCs' surface. The degree of preferential adsorption of CO on (100) sites to that on (110) sites is expressed as the ratio (R) of $\eta_{(100)\ sites}$ over $\eta_{(110)\ sites}$, i.e.,

$$R = \frac{\eta_{(100)\ sites}}{\eta_{(110)\ sites}} \qquad (4)$$

R stands for the priority of CO adsorption on (100) sites. The larger the value of R, the more priority of CO adsorption on (100) sites. The CO coverage dependence of R for all electrodes investigated are compared in Fig. 3. For the THH Pt NCs, R is very large at low θ_{co}, and decreased with the increase of θ_{co}, e.g., 41.6 at $\theta_{co} = 0.135$ and 5.5 at $\theta_{co} = 0.175$.

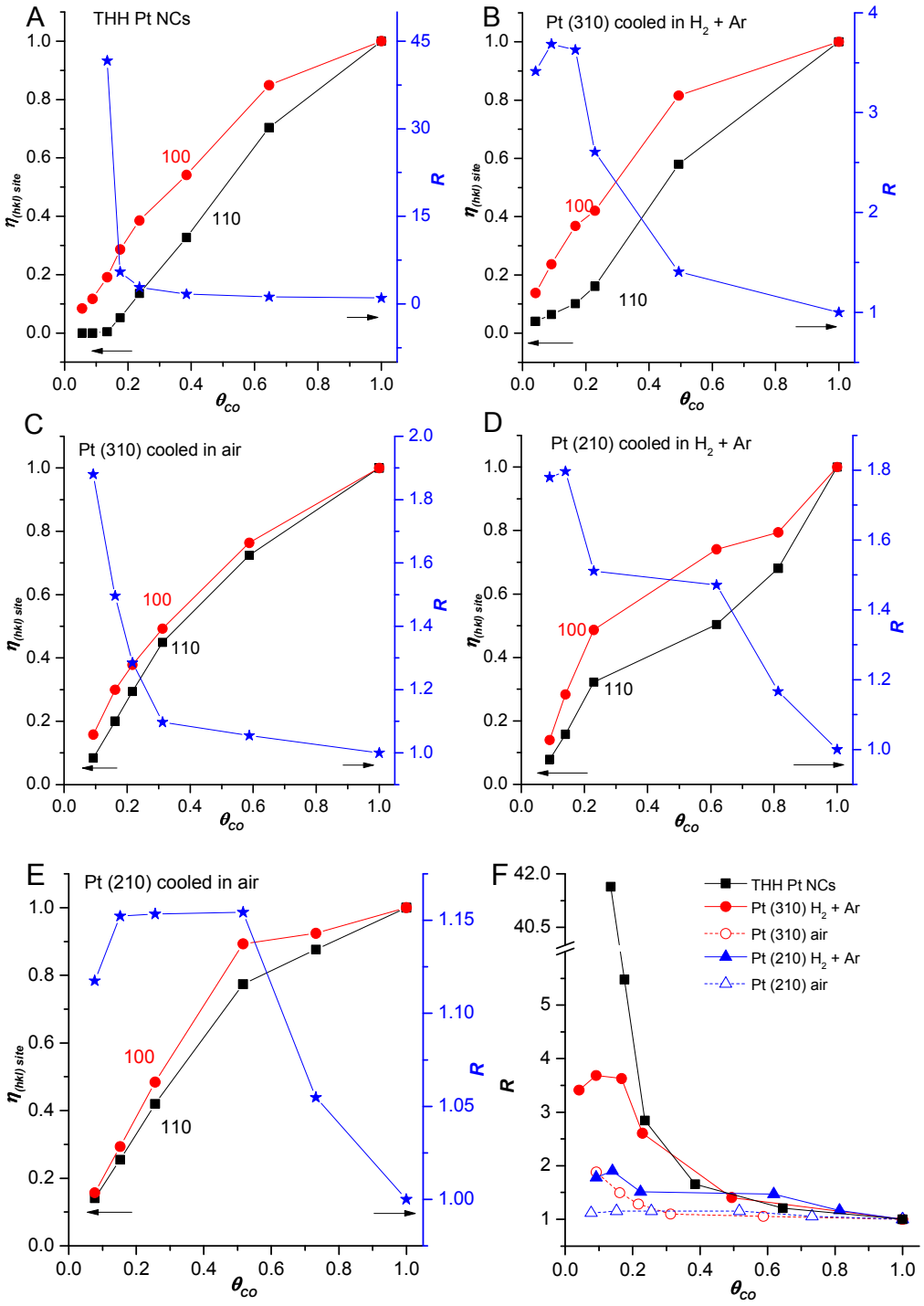

Fig. 3 Coverage dependence of $\eta_{(hkl)sites}$ and *R* on THH Pt NCs (A), Pt(310) cooled in H_2 + Ar (B), Pt(310) cooled in air (C), Pt(210) cooled in H_2 + Ar (D), and Pt(210) cooled in air (E). Comparison of *R* measured on all investigated electrodes (F).

For Pt(310) and Pt(210) single crystal electrodes cooled in H_2 + Ar or in air after flame

annealing, as show in Fig. 3B−E, the values of $\eta_{(100)\ sites}$ are always bigger than those of $\eta_{(110)\ sites}$, and the *R* occurs in a decreasing trend with the increase of θ_{co}. The Pt(310) cooled in H_2 + Ar (Fig. 3B) demonstrates the largest difference between $\eta_{(100)\ sites}$ and $\eta_{(110)\ sites}$, and therefore it has the largest *R* among all the single crystal electrodes studied. For the ordered Pt(310), *R* is 3.6 at $\theta_{co} \leq$ 0.167 and 1.9 at θ_{co} =0.092, while *R* is about 1.5 at θ_{co} = 0.162 for oxygen-defected Pt(310). When $\theta_{co} \leq 0.14$ the *R* is about 1.8 measured on the ordered Pt(210), but the *R* is near to 1 for the oxygen-defected Pt(210), which indicates that there is almost no priority of CO adsorption on (100) sites on the oxygen-defected Pt(210) electrode.

The variations of *R* against θ_{co} for all electrodes investigated are compared in Fig. 3F. It is clear that at low CO coverage ($\theta_{co} < 0.2$) the THH Pt NCs electrode has the largest *R* value among all the electrodes. The preferential adsorption of CO on (100) sites for all electrodes is decreased in an order of THH Pt NCs > ordered Pt(310) > oxygen-defected Pt(310) ≈ ordered Pt(210) > oxygen-defected Pt(210). It is interesting to see that the *R* values of ordered Pt(310) and Pt(210) are always larger than those of oxygen-defected Pt(310) and Pt(210), respectively, indicating that a high *R* value corresponds to a more ordered surface. These results imply that the small facets on the surface of THH Pt NCs is even more ordered than that of Pt(310) and Pt(210) single crystal planes.

3.2 In-situ FTIR Spectroscopic Studies

CO adsorption on THH Pt NCs and Pt (310) single crystal electrode are further studied by using in-situ FTIR spectroscopy. The CO coverage in the in-situ FTIR studies was defined as,

$$\theta_{CO}^{IR} = \frac{I_{CO}^{COL} + I_{CO}^{COB}}{I_{1ML-CO}^{COL} + I_{1ML-CO}^{COB}} \qquad (5)$$

In which the I_{CO}^{COL} and I_{CO}^{COB} are integrated intensity of the IR bands of CO_L and CO_B at different coverage, respectively. I_{1ML-CO}^{COL} and I_{1ML-CO}^{COB} are integrated intensity of the IR bands of CO_L and CO_B for CO saturation adsorption (one monolayer CO).

The in-situ FTIR spectra of CO adsorption on the THH Pt NCs with a high distribution density of 60 μm^{-2} display obviously three IR bands as illustrated in Fig. 4A. One band between 2000 and 2100 cm^{-1} and another one around 1782 cm^{-1} are assigned respectively to linearly bonded CO

(CO_L) and bridge coordinated CO (CO_B) species according to the previous study.[30] The positive-going band around 2343 cm^{-1} is attributed to IR absorption of solution CO_2 species produced solely from CO_{ad} oxidation at reference potential (0.75 V). From the definition of in-situ FTIR spectra by the equation (2), the IR absorption of CO_{ad} at E_S should yield negative-going bands. However, the CO_B band is on the opposite direction of negative-going, and the CO_L band appears in asymmetric bipolar shape with enhanced intensity. These are typical anomalous IR effects (AIREs) of nanomaterials for CO adsorption,[31-34] among which the asymmetric CO_L bipolar IR band has been denoted as Fano-like IR spectral line shape.[34]

Fig. 4B demonstrates the IR band intensity of CO_L (I_{COL}) and CO_B (I_{COB}) measured in spectra of THH Pt NCs of high distribution density. I_{COL} is weaker than I_{COB} at very low CO coverage (θ_{CO}^{IR} = 0.029), but I_{COL} increases quickly than I_{COB}, yielding a linear variation with the increase of CO coverage. In contrast, the I_{COB} decreases at θ_{CO}^{IR} > 0.184. Since CO_L can adsorb on both (100) sites or (110) sites and CO_B adsorbed mainly on Pt(100) sites, the amount of CO_B adsorbed on Pt(100) sites is certainly larger than that of CO_L on Pt(110) sites at CO coverage of 0.029. We can thus conclude that CO prefers to adsorb on Pt(100) sites at very low CO coverage of 0.029.

The IR band center of CO_L shifts to high wavenumbers with the increase of CO coverage, as can be seen in Fig. 4C. With the increase of CO coverage, CO_L band blue shifts linearly and quickly from 2006 cm^{-1} to 2040cm^{-1} when $\theta_{co}^{IR} \leq 0.184$, and produced a big slope about 219 cm^{-1}. When θ_{co}^{IR} > 0.184; the increase of the band center of CO_L is deviated from the linearity and increased relatively slowly from 2040 cm^{-1} to 2075 cm^{-1} as the CO coverage increases from 0.184 to 1. This demonstrates that the behavior of CO adsorption is different for θ_{co}^{IR} < 0.184 and θ_{co}^{IR} > 0.184. From IR spectra (Fig. 4A), the broad positive branch of the asymmetric bipolar CO_L band could be deconvoluted into two peaks, as illustrated in the inset (a) for the spectrum of θ_{co}^{IR} = 0.255. In the spectrum of θ_{co}^{IR} = 0.184 we indeed can discern two CO shoulder peaks (2007 and 2027 cm^{-1}) on CO_L bands. According to previous reports[26] the spectral bands for CO_L adsorbed on (100) steps are ca. 10 cm^{-1} red-shifted with respect to those for CO on (110) steps at all CO fractional coverages. For the {730} facets on THH Pt NCs, the width of (100) terrace is quite narrow, the (100) sites on THH Pt NCs behaviors essentially as (100) step, as evidenced by the hydrogen adsorption-desorption peaks at −0.02 V in cyclic voltammogram (Fig. 1C). The

observed CO shoulder peaks at low and high wavenumbers can be assigned to CO_L on (100) sites and (110) sites, respectively. At CO coverage higher than 0.184, the amount of CO_L on (110) sites increases obviously. These FTIR results are consistent with those obtained from cyclic voltammetric studies.

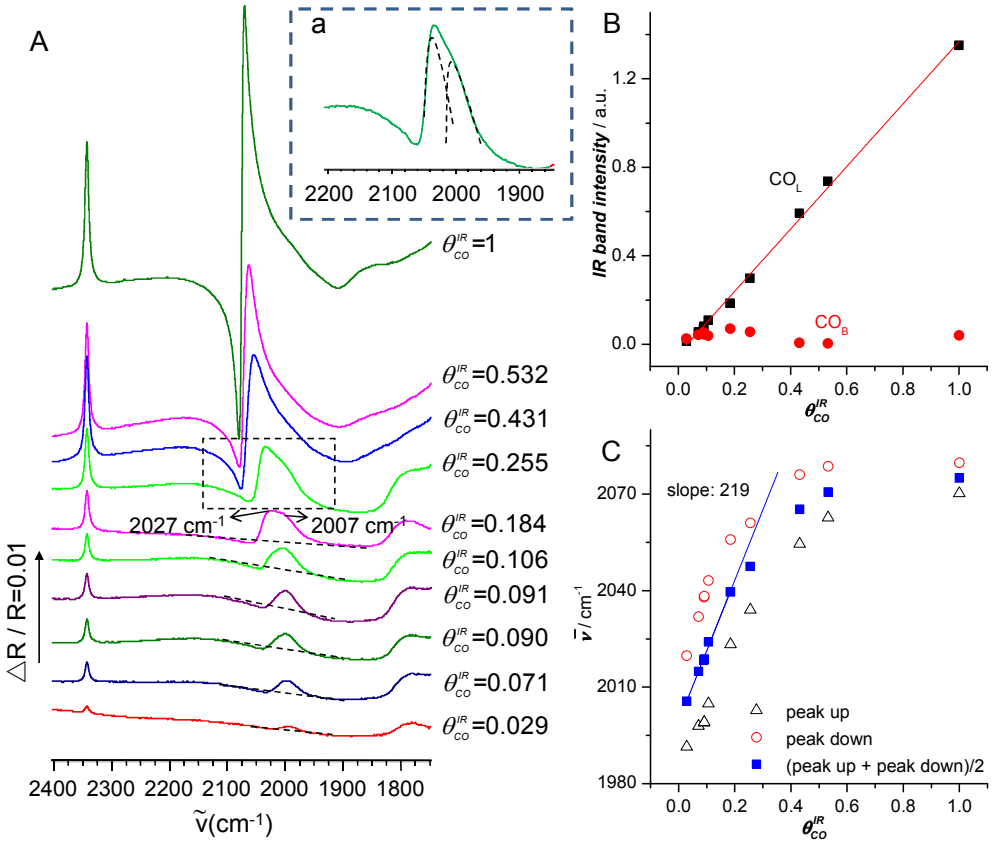

Fig. 4 (A) Coverage dependence of in-situ FTIR spectra for CO adsorbed on THH Pt NCs of high distribution density (60 μm^{-2}) in 0.1 M $HClO_4$ solution, E_S = −0.10 V, E_R = 0.75 V (SCE). (B) Coverage dependence of band intensities of CO_L and CO_B on THH Pt NCs in Fig. 4A. (C) The IR band center of CO_L plotted against the coverage of CO (θ_{CO}^{IR}) in Fig. 4A, hollow dark triangles present the center of positive peak of CO_L asymmetric bipolar band; the hollow red circles stand for the center of negative peak of CO_L asymmetric bipolar band; and the filled blue squares is the average wavenumber of the centers of positive and the negative peaks.

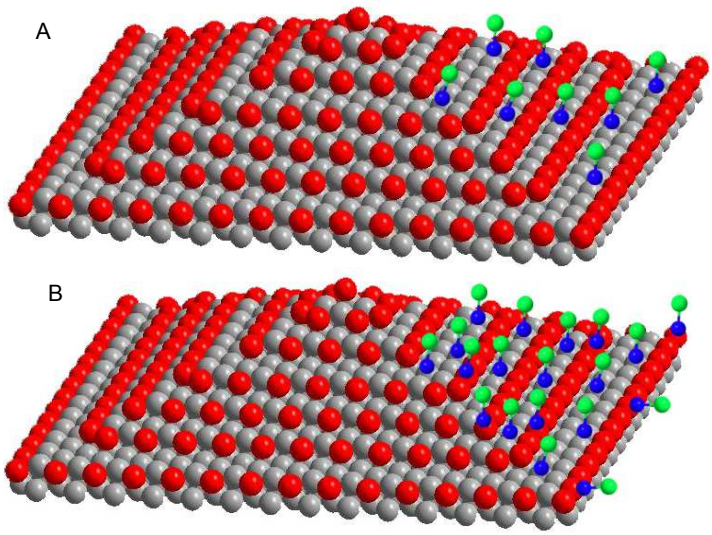

Fig. 5 The models of low coverage (A) and high coverage (B) of CO adsorbed on the surface of THH Pt NCs (only a half square pyramid of the THH Pt NCs is shown. And red: steps; grey: terraces; blue: C, green: O.).

From above results, we may propose models for CO adsorption at different coverage. As presented in Fig. 5A, at lower coverage of CO, both CO_L and CO_B adsorbed on (100) sites. Along with increasing the coverage of CO (Fig. 5B), CO_L and CO_B adsorbed on both (100) and (110) sites, and the amount of CO_L is larger than that of CO_B.

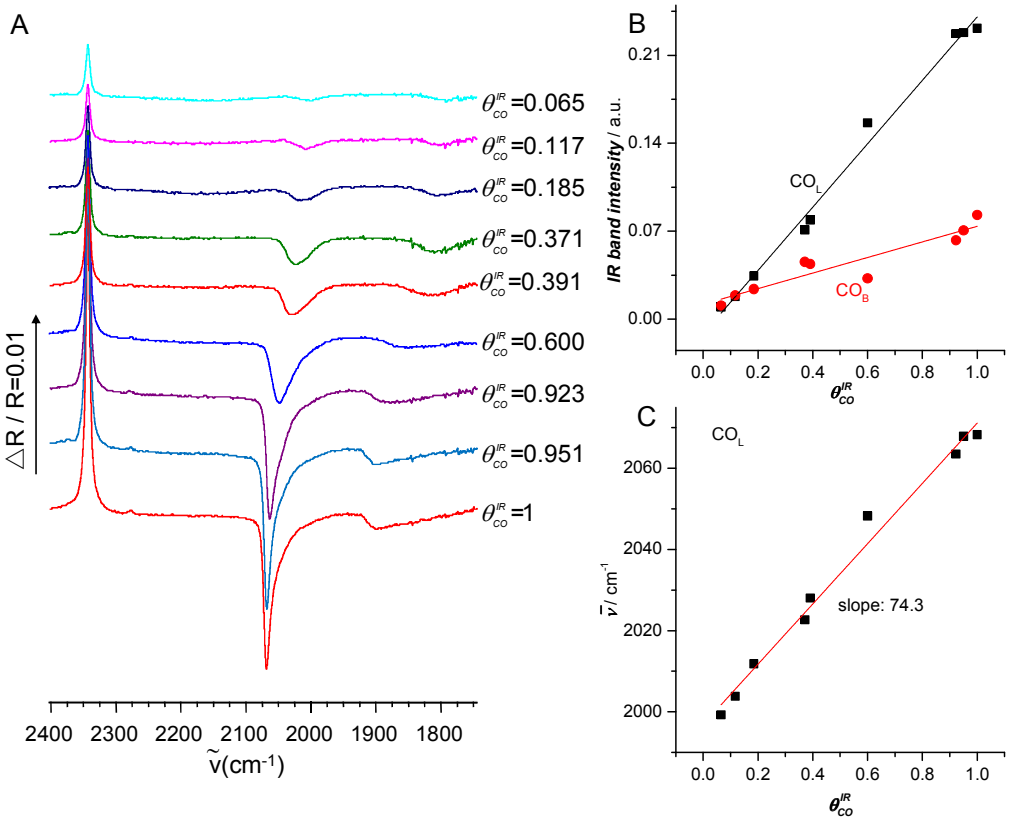

Fig. 6 (A) Coverage dependence of in-situ FTIR spectra for CO adsorbed on Pt (310) cooled in air after flame treatment, in 0.1 M $HClO_4$ solution, E_S = −0.10 V, E_R = 0.60 V (SCE). (B) Coverage dependence of the band intensity of CO_L and CO_B in air in (A). (C) IR band center of CO_L plotted against the coverage of CO_L and CO_B.

The in-situ FTIR spectra of CO adsorption on Pt(310)cooled in air after flame treatment with different CO coverage at −0.10 V are displayed in Fig. 6A. The negative-going band at 2002 and 1798 cm^{-1} can be assigned as CO_L and CO_B, respectively, and the positive-going band around 2343 cm^{-1} is attributed to IR absorption of solution CO_2 species produced by CO oxidation at reference potential (0.60 V). It is evident that the IR features of CO adsorption on a bulk electrode are normal, i.e. the direction of IR bands of adsorbed CO follows the in-situ FTIR spectra definition of equation (2).

As presented in Fig. 6B, the IR band intensities of I_{COL} and I_{COB} on Pt(310) single crystal electrode cooled in air are almost linearly increased with the increase of θ_{CO}^{IR}. At low CO coverage

($\theta_{co}^{IR} \leq 0.117$), I_{COL} is nearly equal to I_{COB}, but I_{COL} is quickly increased with the increase of θ_{co}^{IR}. while I_{COB} is increased slowly. Fig. 6C shows the variation of IR band centers of CO_L and CO_B against the CO coverage in the whole θ_{co}^{IR} range. Along with increasing the CO coverage, the CO_L band center is linearly blue shifted from 1998cm^{-1} to 2070cm^{-1}, producing a slope about 74.3 cm^{-1} that is only about one third of the value obtained on THH Pt NCs. The fact that the IR band centers of both CO_L and CO_B linearly blue shift with the increase of CO coverage in the whole CO coverage indicates that CO_L adsorbs homogeneously on (100) and (110) sites of Pt(310), which is consistent with the results from studies of cyclic voltammetry.

4. Discussions

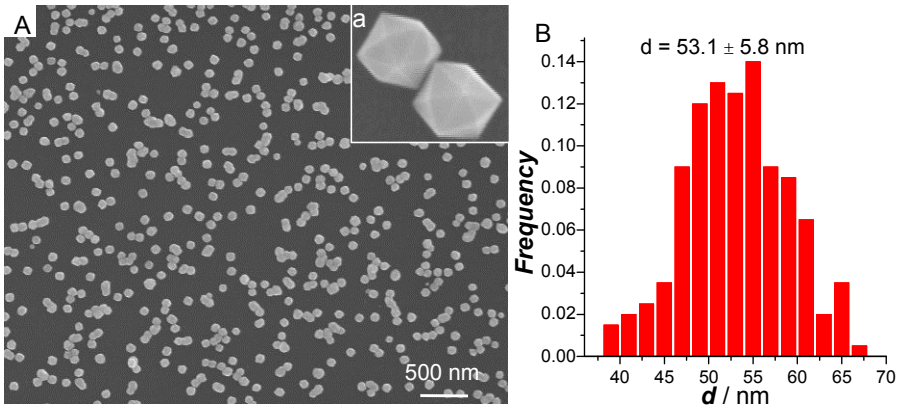

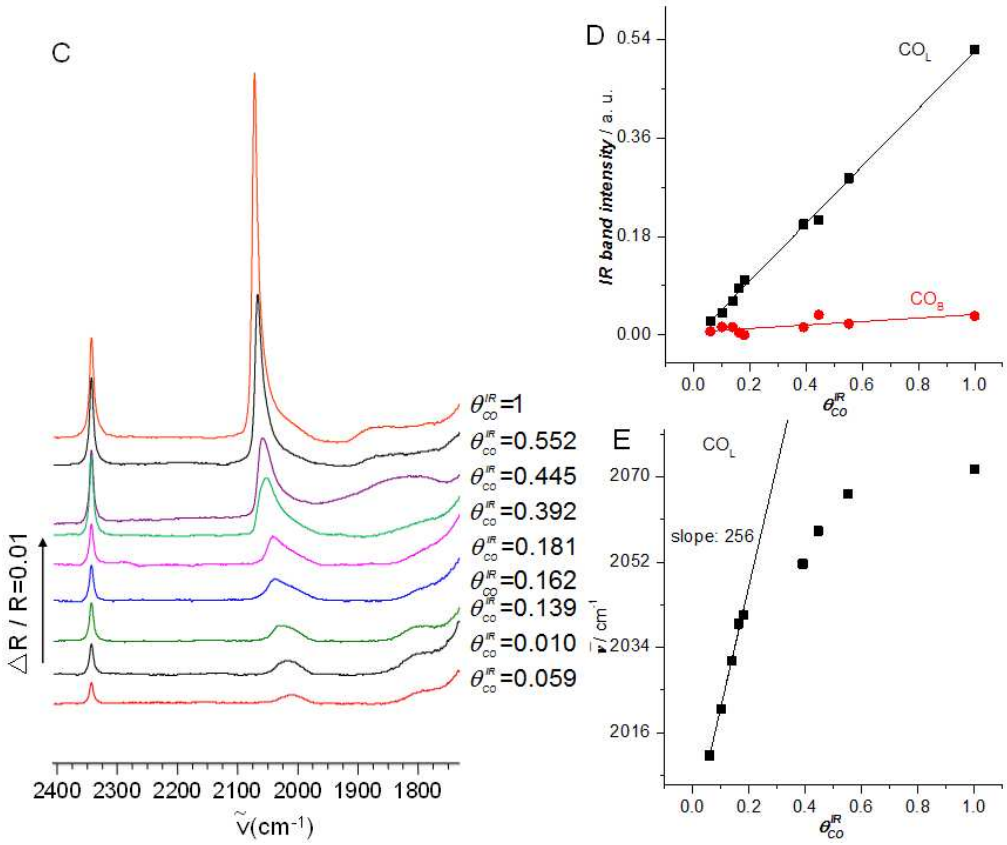

Fig. 7 (A) SEM image of THH Pt NCs with relatively low distribution density of 22 μm^{-2}. The inset (a) is a high magnification image of the sample and illustrates clearly the characteristic THH shape. (B) Size distribution histogram of the THH Pt NCs. (C) Coverage dependence of in-situ FTIR spectra for CO adsorbed on THH Pt NCs electrode in 0.1 M $HClO_4$ solution, E_S = −0.10 V, E_R = 0.75 V. (D) Coverage dependence of IR band intensity of CO_L and CO_B on THH Pt NCs in Fig. 7C. (E) IR band center of CO_L plotted against θ_{co}^{IR} in Fig. 7C.

As shown in Fig. 4, the in-situ FTIR spectra of CO_{ad} on THH Pt NCs with distribution density of 60 μm^{-2} demonstrate asymmetric bipolar IR features and the center of the CO_L band increasing nonlinearly with the increase of CO coverage. As the anomalous IR effects of nanoparticles depends strongly on aggregation state of nanomaterials,[31, 35] we have also prepared THH Pt NCs with relatively low distribution density of about 22 μm^{-2}. The mean size of the THH Pt NCs is about 53 nm that is similar to the THH Pt NCs of high distribution density studied above. The high magnification of the sample and the size distribution histogram are illustrated in Fig.7A and Fig. 7B, respectively.

Fig. 7C displays the in-situ FTIR spectra of CO adsorbed on THH Pt NCs with low distribution density at −0.10 V at different CO coverage. The positive-going bands around 2010 and 1805 cm^{-1} are assigned to CO_L and CO_B, respectively. Interestingly, the CO_L on the THH Pt NCs with low distribution density yields only abnormal enhanced IR band and losses the "Fano-like" IR feature of asymmetric bipolar line shape. The positive band around 2343 cm^{-1} is ascribed to IR absorption of solution CO_2 species produced by CO oxidation at reference potential (0.75V).

As presented in Fig. 7D, the IR band intensity of I_{COL} and I_{COB} in the spectra of CO adsorbed on THH Pt NCs with low distribution density are both increased linearly with the increase of θ_{co}^{IR}. This is different from the variations of I_{COL} and I_{COB} in the spectra of CO adsorbed on the THH Pt NCs with high distribution density (shown in Fig. 4B). Although the I_{COL} is still much larger than I_{COB} and gives a fast linear increase with the increase of θ_{co}^{IR}, the I_{COB} keeps a slow and linear increase in the whole θ_{co}^{IR} range.

The variation of the IR band center of CO_L with the increase of CO coverage is shown in Fig. 7E. We observe similar variation tend as that presented in Fig. 4C for CO adsorption on THH Pt NCs with high distribution density. The CO_L band center is linearly blue shifted from 2010 cm^{-1} to 2040 cm^{-1} for $\theta_{CO}^{IR} < 0.181$, yielding still a big slope about 256 cm^{-1}. When $\theta_{co}^{IR} > 0.181$, the increase of the CO_L band center is deviated from the linearity, and becomes slow and nonlinear. The CO_L band center increased from 2040 cm^{-1} to 2070 cm^{-1} along with the increase of θ_{CO}^{IR} from 0.181 to 1. These results demonstrate that the THH Pt NCs have anomalous IR effects for CO adsorption, and the anomalous IR features depend on the distribution density of the THH Pt NCs on GC substrate. Although it is difficult to discern clearly two shoulder peaks on THH Pt NCs with low distribution density in the spectra displays in Fig. 7A, the CO_L bands are obviously broadened at CO coverage larger than 0.181.

Compared to the linearly blue shift of the CO_L band center with the increase of CO coverage on Pt (310) electrode cooled in air, the changing tendency of CO adsorption on THH Pt NCs has two stages. For the first stage of CO adsorption ($\theta_{co}^{IR} < 0.181$), the slope was 256 cm^{-1} on THH Pt NCs with low distribution density of 22 μm^{-2} (Fig. 7E) and 219 cm^{-1} on THH Pt NCs with high distribution density of 60 μm^{-2} (Fig. 4C), both are much larger than that on Pt(310) electrode cooled in air (only 74.3cm^{-1}, Fig. 6C). As stated above, on THH Pt NCs CO dominantly adsorbed

on (100) sites at θ_{CO}^{IR} < 0.181, while CO adsorbed on both (100) and (110) sites on Pt(310) electrode cooled in air. For a given low CO coverage, the local CO coverage on THH Pt NCs should be larger than that on Pt(310) electrode cooled in air. For CO adsorption on Pt, there is dipole-dipole interaction of neighbored CO, which can decrease the d-π* back donation. This consequently enhances the $C \equiv O$ bond and weakens the CO adsorption, as well as increasing the frequency of CO stretching vibration.[36] The dipole-dipole interaction of neighbored CO increases with the increase of CO coverage, resulting in the blue shift of CO band with increasing coverage. The dipole-dipole interaction should be much stronger on THH Pt NCs than on Pt(310) electrode cooled in air, which may be ascribed to the relatively higher local CO coverage and the particularity of the nanosize, corner and edge sites on the THH Pt NCs.

The frequency of CO_L band is different for different samples. For CO coverage of ~ 0.2, the band center of CO_L are at 2042 and 2047 cm^{-1} on THH Pt NCs with both high and low distribution density, respectively, while it is only 2012 cm^{-1} on Pt(310) single crystal cooled in air. These differences can also be explained by the stronger dipole-dipole interaction of neighbored CO on THH Pt NCs. Another factor may be due to the confinement of facet in nanosize and the local environment (corner and edge sites) difference between nanoparticles and single crystal plane.

The preferential adsorption of CO on all electrodes investigated is decreased in an order of: THH Pt NCs > Pt (310) cooled in H_2 + Ar > Pt(310) cooled in air ≈ Pt(210) cooled in H_2 + Ar > Pt(210) cooled in air. For Pt(210) cooled in air, there was no preferential adsorption on different sites, referring to the results of Feliu group[22] and Kim et al.[37] Feliu group investigated the behavior of CO adsorption on Pt high-index single crystal planes of (776) and (554) and low-index (111) plane, and demonstrated that CO adsorbed on terraces and steps randomly.[22] They also investigated CO adsorption on well-defined Pt nanoparticles enclosed with low-index facets (including cubes, octahedral tetrahedral nanoparticles, truncated octahedral and tetrahedral nanoparticles with size of about 4 ~ 5 nm) in alkaline conditions,[38] and found that there are no preferential adsorption of CO on different surface sites. The significant priority of CO adsorption on (100) sites on THH Pt NCs manifests an exceptional property of high-index facets at nanoscale size.

The IR features are different for THH Pt NCs with low distribution density and those with high

distribution density. With the increase of the distribution density of THH Pt NCs, the IR band of CO_L transformed from abnormal enhancement IR features (distribution density of 22 μm^{-2}) to Fano-like IR features (distribution density of 60 μm^{-2}). Since the size of THH Pt NCs is similar, this transition should relate to difference of the distribution density of THH Pt NCs. Our previous results of Co nanoparticles[34] demonstrated that with the growth of nanoparticles, the IR band is changed from abnormal enhancement IR features to Fano-like IR features, and finally to enhanced IR absorption features. The anomalous IR effects are peculiar for nanostructure materials, which usually relate with the structure, size and distribution density of the nanoparticles.

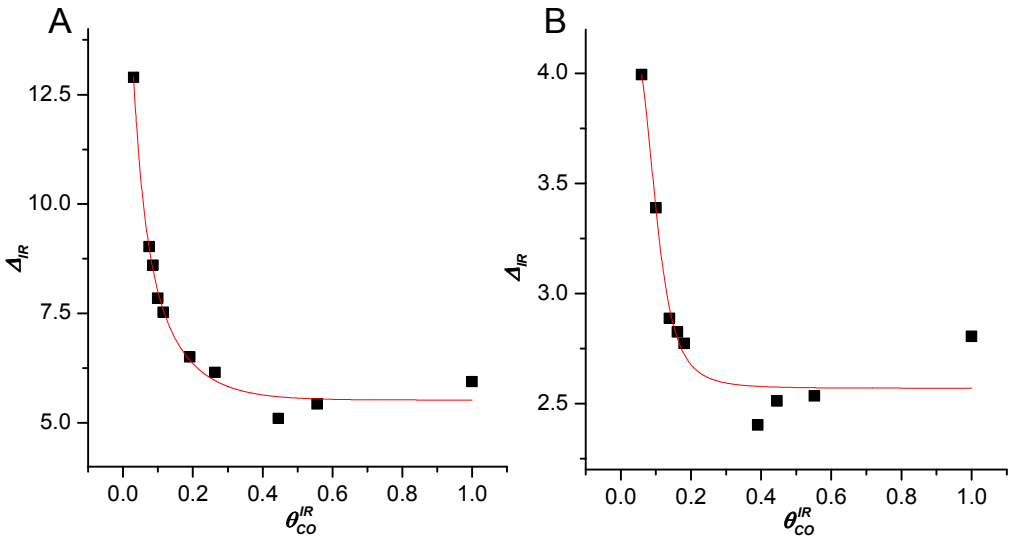

Fig. 8 Coverage dependence of IR enhancement factor (Δ_{IR}) on THH Pt NCs with high distribution density (A) and low distribution density (B).

The IR absorption of CO_L on THH Pt NCs has been significantly enhanced. The IR enhancement factor (Δ_{IR}) is defined as:

$$\Delta_{IR} = \frac{\left[\frac{I_{COL}+I_{COB}}{I_{CO2}}\right]_{THH}}{\left[\frac{I_{COL}+I_{COB}}{I_{CO2}}\right]_{Pt(310)}} \qquad (6)$$

Fig. 8 displays the coverage dependence of Δ_{IR} for THH Pt NCs with high and low distribution densities. Δ_{IR} decreases hyperbolically against the increase of CO coverage on THH Pt NCs with both high and low distribution density, while the Δ_{IR} of the former is larger than that of the later

one. The highest value of Δ_{IR} for THH Pt NCs electrode with high distribution density is about 12.8 at the lowest CO coverage (θ_{CO}^{IR} = 0.029). Δ_{IR} decreases sharply with the increase of CO coverage, drops to about 5.6 at CO coverage of 0.445, and then keeps stable with further CO coverage increasing. However, for the THH Pt NCs with low distribution density, Δ_{IR} is only 4.0 at the lowest CO coverage (θ_{CO}^{IR} = 0.059), and then is sharply decreased with the increase of CO coverage. It decreases to about 2.8 at θ_{CO}^{IR} = 0.181, and then reaches progressively steady of about 2.6 with the increase of CO coverage. It is evident that the THH Pt NCs of high distribution density has higher IR enhancement factor than that of low distribution density towards CO adsorption.

It should be noted that, in the present paper, the CO coverage (θ_{CO}) used in cyclic voltammetry studies was calculated by taking the ratio of the oxidation charge of submonolayer CO_{ad} to that of one monolayer CO_{ad} (i.e. the saturation adsorption), which is different from that used in Weaver's work[39]. According to ref. 32, the real CO coverage (θ_R) could be expressed as: $\theta_R = \frac{Q_{CO}}{2Q_H}$. The real CO coverage ($\theta_R$) corresponding to θ_{CO} = 1 on all electrodes investigated in Fig. 1 and Fig. 2 were calculated and listed in the table 1. The θ_R corresponding to θ_{CO}= 1 on THH Pt NCs is around 0.8, and it is about 0.7 for θ_{CO}= 1 on Pt (210) and Pt (310) single crystal electrodes.

Table 1: The real CO coverage (θ_R) corresponding to θ_{CO}= 1
on all electrodes investigated in Fig. 1 and Fig. 2

Electrode	θ_R
THH Pt NCs	0.81
Pt(210) cooled in air	0.73
Pt(210) cooled in H_2 + Ar	0.69
Pt(310) cooled in air	0.67
Pt(310) cooled in H_2 + Ar	0.69

For the θ_{CO}^{IR} denoted in the FTIR spectra, it is calculated according to the formula (5). Since at different CO coverage the CO_L band show different IR enhancement (Fig. 8), the "real" CO

coverage (θ_R^{IR}) should be different. The θ_R^{IR} can be calculated by taking into account the influence of IR enhancement factor, at the same time omitting the contribution of CO_B (since its intensity is quite low), by using the following formula:

$$\theta_R^{IR} = \frac{I_{CO}^{COL} / \Delta_{IR-CO}}{I_{1ML-CO}^{COL} / \Delta_{IR-1ML-CO}} \quad (7)$$

The θ_R^{IR} calculated is listed in table 2.

Table 2: The real CO coverage (θ_{CO}^{IR}) for the THH Pt NCs with different distribution density in Fig. 4 and Fig. 7.

THH Pt NCs of high distribution density (60 μm^{-2})		THH Pt NCs of low distribution density (22 μm^{-2})	
θ_{CO}^{IR}	θ_R^{IR}	θ_{CO}^{IR}	θ_R^{IR}
0.029	0.012	0.059	0.038
0.071	0.043	0.100	0.076
0.090	0.058	0.139	0.123
0.091	0.064	0.162	0.147
0.106	0.079	0.181	0.168
0.184	0.159	0.391	0.388
0.255	0.234	0.445	0.445
0.431	0.428	0.552	0.552
0.532	0.532	1	1
1	1		

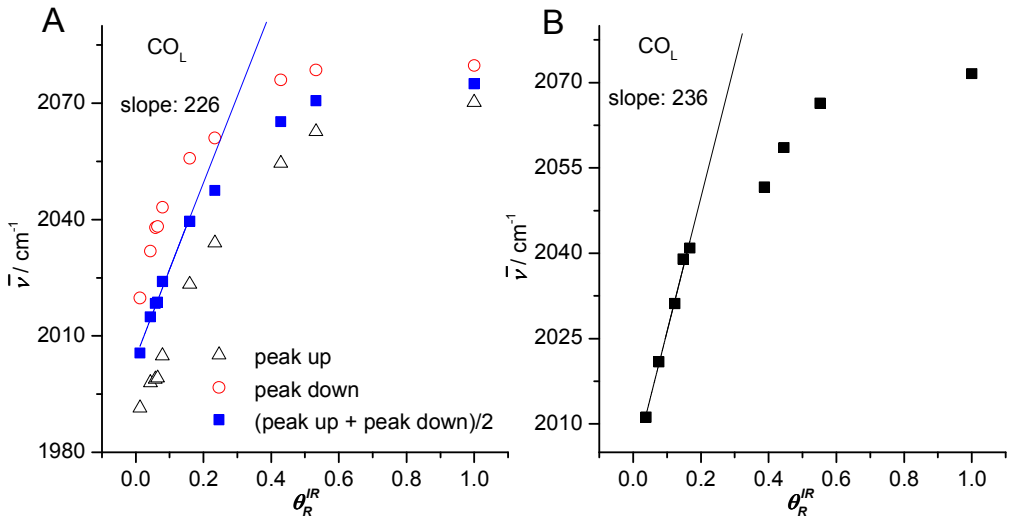

Fig. 9 IR band center of CO_L plotted against θ_R^{IR} for THH Pt NCs with high distribution density (60 μm^{-2}) (A), and low distribution density (22 μm^{-2}) (B). In A, the hollow dark triangles represent the positive peak of the asymmetric bipolar CO_L band; the hollow red circles stand for the negative peak of the asymmetric bipolar CO_L band; and the filled blue squares are the average wavenumbers of the positive and the negative peak.

Fig. 9 demonstrates the IR band center of CO_L plotted against θ_R^{IR} for THH Pt NCs electrode with high distribution density (60 μm^{-2}) and low distribution density (22 μm^{-2}). The calibration of the CO coverage changes slightly the slope. For THH Pt NCs with high distribution density (60 μm^{-2}) the slope has increased from 219 to 226 cm^{-1}, and it decreased from 256 to 236cm^{-1} for THH Pt NCs with low distribution density (22 μm^{-2}).

5. Conclusions

We investigated CO adsorption on THH Pt NCs and interrelated Pt single crystal planes by electrochemical cyclic voltammetry and in-situ FTIR spectroscopy. The results revealed that CO adsorption on Pt THH NCs exhibits significant priority on (100) sites at low CO coverage. The preferential adsorption of CO on (100) sites decreases in an order of Pt THH NCs > Pt(310) cooled in H_2 + Ar > Pt (310) cooled in air ≈ Pt(210) cooled in H_2 + Ar > Pt(210) cooled in air.

The in-situ FTIR study demonstrates that, in comparison with Pt(310) singe crystal electrode, the THH Pt NCs exhibit anomalous IR effects (AIREs) towards CO adsorption. The anomalous IR

features of CO_{ad} depend on the distribution density of THH Pt NCs, and are transformed from enhancement of abnormal IR absorption (22 μm^{-2}) to Fano-like IR spectral line shape (60 μm^{-2}) along with increasing the distribution density. The coverage-dependent vibration frequency of CO_L on THH Pt NCs demonstrates two segments. The center of CO_L band is blue shifted quickly and linearly with the increase of CO coverage when $\theta_{CO}^{IR} < 0.18$, yielding a big slope of 219, and then deviated from the linearity and is approaching finally to steady variation for $\theta_{CO}^{IR} > 0.18$. The variation of the band center of CO_L band on Pt(310) cooled in air is quite different. Which manifests a linear relationship for the whole range of θ_{CO}^{IR} and gives a much smaller slop of 74.3. The significant priority of CO adsorption on (100) sites of THH Pt NCs and the AIREs of the THH Pt CNs demonstrate the unique properties of the THH Pt NCs that are significantly different from the interrelated single crystal planes of Pt(310) and Pt(210). The unique properties are ascribed to the confinement of the Pt high-index planes into nanosized facets, the particular corners and edges sites on the surface of high-index faceted nanoparticles. The results in this paper have enriched the understanding of surface structure effects of Pt nanocrystals enclosed with high-index facets.

Acknowledgments

This study was supported by the National Basic Research Program of China (2012CB215500), NSFC (21222310, 21373175, 21361140374, 21321062, and 21229301), and foundation for the Author of National Excellent Doctoral Dissertation of China (201126).

References

1. Z.-Y. Zhou, N. Tian, J.-T. Li, I. Broadwell and S.-G. Sun, *Chemical Society reviews*, 2011, **40**, 4167-4185.
2. Z. Quan, Y. Wang and J. Fang, *Accounts of Chemical Research*, 2012, **46**, 191-202.
3. N. Tian, Z. Y. Zhou, S. G. Sun, Y. Ding and Z. L. Wang, *Science*, 2007, **316**, 732-735.
4. N. Tian, Z. Y. Zhou, N. F. Yu, L. Y. Wang and S. G. Sun, *Journal of the American Chemical Society*, 2010, **132**, 7580-7581.
5. N. F. Yu, N. Tian, Z. Y. Zhou, L. Huang, J. Xiao, Y. H. Wen and S. G. Sun, *Angewandte Chemie International Edition*, 2014, **53**, 5097-5101.
6. Y. Y. Li, Y. X. Jiang, M. H. Chen, H. G. Liao, R. Huang, Z. Y. Zhou, N. Tian, S. P. Chen and S. G. Sun, *Chemical Communications*, 2012, **48**, 9531-9533.
7. N. Tian, Z.-Y. Zhou and S.-G. Sun, *The Journal of Physical Chemistry C*, 2008, **112**,

19801-19817.

8. J. Xiao, S. Liu, N. Tian, Z. Y. Zhou, H. X. Liu, B. B. Xu and S. G. Sun, *Journal of the American Chemical Society*, 2013, **135**, 18754-18757.
9. Y. J. Deng, N. Tian, Z. Y. Zhou, R. Huang, Z. L. Liu, J. Xiao and S. G. Sun, *Chemical Science*, 2012, **3**, 1157-1161.
10. N. Tian, J. Xiao, Z. Y. Zhou, H. X. Liu, Y. J. Deng, L. Huang and B. B. X. a. S. G. Sun*, *Faraday Discuss* . , 2013, **162**, 77-89.
11. N. Hoshi, O. Koga, Y. Hori and T. Ogawa, *Journal of Electroanalytical Chemistry*, 2006, **587**, 79-85.
12. C. Fan, Y. Fan, C. Zhen, Q. Zheng and S. Sun, *Science in China Series B: Chemistry*, 2007, **50**, 593-598.
13. F. J. Vidal-Iglesias, J. Solla-Gullón, J. M. Campiña, E. Herrero, A. Aldaz and J. M. Feliu, *Electrochimica Acta*, 2009, **54**, 4459-4466.
14. S. G. Sun, *Chapter in Electrocatalysis, Edited by J. Lipkowski and P.N. Ross, Wiley-VCH, Inc*, 1998, 243-290.
15. Y. J. Fan, Z. Y. Zhou, C. H. Zhen, S. P. Chen and S. G. Sun, *Electrochemistry Communications*, 2011, **13**, 506-508.
16. F. Illas, F. Mele, D. Curulla, A. Clotet and J. M. Ricart, *Electrochimica Acta*, 1998, **44**, 1213-1220.
17. G. F. Cabeza, N. J. Castellani and P. Legare, *Surface Review and Letters*, 1999, **6**, 369-381.
18. M. J. S. Farias, E. Herrero and J. M. Feliu, *Journal of Physical Chemistry C*, 2013, **117**, 2903-2913.
19. M. J. S. Farias, C. Busó-Rogero, R. Gisbert, E. Herrero and J. M. Feliu, *The Journal of Physical Chemistry C*, 2014, **118**, 1925-1934.
20. S. C. Chang and M. J. Weaver, *Surface Science*, 1990, **238**, 142-162.
21. S. C. Chang and M. J. Weaver, *J. Phys. Chem.*, 1991, **95**, 5391-5400.
22. M. J. S. Farias, A. A. Tanaka, G. Tremiliosi and J. M. Feliu, *Electrochemistry Communications*, 2011, **13**, 338-341.
23. J. Clavilier, D. Aemand, S. G. Sun and M. Petit, *Journal of Electroanalytical Chemistry*, 1986, **205**, 267-277
24. T. Biegler, D. A. J. Rand and R. Woods, *Journal of Electroanalytical Chemistry and Interfacial Electrochemistry*, 1971, **29**, 269-277.
25. S. G. Sun and Y. Lin, *Electrochimica Acta*, 1998, **44**, 1153-1162.
26. N. P. Lebedeva, A. Rodes, J. M. Feliu, M. T. M. Koper and R. A. van Santen, *Journal of Physical Chemistry B*, 2002, **106**, 9863-9872.
27. N. P. Lebedeva, M. T. M. Koper, J. M. Feliu and R. A. van Santen, *The Journal of Physical Chemistry B*, 2002, **106**, 12938-12947.
28. F. J. Vidal-Iglesias, J. Solla-Gullon, J. M. Campina, E. Herrero, A. Aldaz and J. M. Feliu, *Electrochimica Acta*, 2009, **54**, 4459-4466.
29. L. A. Kibler, A. Cuesta, M. Kleinert and D. M. Kolb, *Journal of Electroanalytical Chemistry*, 2000, **484**, 73-82.
30. K. Mikita, M. Nakamura and N. Hoshi, *Langmuir : the ACS journal of surfaces and colloids*, 2007, **23**, 9092-9097.
31. G. Q. Lu, S. G. Sun, L. R. Cai, S. P. Chen, Z. W. Tian and K. K. Shiu, *Langmuir : the ACS*

journal of surfaces and colloids, 2000, **16**, 778-786.

32. H. Gong, S. G. Sun, Y. J. Chen and S. P. Chen, *The Journal of Physical Chemistry B*, 2004, **108**, 11575-11584.
33. H. C. Wang, S. G. Sun, J. W. Yan, H. Z. Yang and Z. Y. Zhou, *The Journal of Physical Chemistry B*, 2005, **109**, 4309-4316.
34. Q. S. Chen, S. G. Sun, J. W. Yan, J. T. Li and Z. Y. Zhou, *Langmuir : the ACS journal of surfaces and colloids*, 2006, **22**, 10575-10583.
35. Y. X. Jiang, S. G. Sun and N. Ding, *Chemical Physics Letters*, 2001, **344**, 463-470.
36. S. C. Chang and M. J. Weaver, *Journal of Chemical Physics*, 1990, **92**, 4582-4594.
37. C. S. Kim and C. Korzeniewski, *Analytical Chemistry*, 1997, **69**, 2349-2353.
38. M. J. S. Farias, F. J. Vidal-Iglesias, J. Sola-Gullon, E. Herrero and J. M. Feiu, *Journal of Electroanalytical Chemistry*, 2014, **716**, 16-22.
39. R. Gómez, J. M. Feliu, A. Aldaz and M. J. Weaver, *Surface Science*, 1998, **410**, 48-61.